ELSEVIER

Materials Science and Engineering B42 (1996) 88–98

MATERIALS SCIENCE & ENGINEERING B

Scanning probe microscopy for 2-D semiconductor dopant profiling and device failure analysis

A.K. Henning*, T. Hochwitz

Thayer School of Engineering, Dartmouth College, Hanover, NH 03755-8000, USA

Abstract

We have extended the capabilities of an atomic force microscope (AFM) with double heterodyne force detection, to include both electrostatic force microscopy (EFM) and scanning differential capacitance microscopy (SdCM). Samples measured with this tool are imaged simultaneously in each of these three modes. Inhomogeneities in surface topography (AFM), surface work function (EFM) and sub-surface charge (SdCM) are thus detected at once. We work in non-contact mode in order to interact non-destructively with our samples, with resultant lateral spatial resolution of 25–50 nm. Variations in surface topography of less than 1 nm, and surface potential variations as small as 1 mV, are imaged easily. We have applied the techniques based on this tool to microfabricated materials and device structures. In particular, we have studied the metal-oxide-silicon field-effect transistor (MOSFET) structure, of importance to microelectronic science and engineering. Following a brief description of our detection system, this work will describe our measurements of dopant profiles related to this structure. It will also demonstrate our ground-breaking application of scanned probe techniques to the analysis of other materials defects, and of device failure, in these structures. The work will conclude with a quantitative discussion of the three most limiting factors for our techniques: parasitic capacitance; convolved signals; and large-signal behavior of the cantilever.

Keywords: Atomic force microscope; Dopant profiling; Electrostatic force microscopy

1. Introduction

Dopant profiling in silicon and gallium arsenide devices on micrometer and sub-micrometer scales has long been a goal for process and device engineers. One-dimensional profile measurement has been available since the middle 1970s. However, in silicon bipolar, silicon MOSFET, and GaAs-related heterostructure devices, accurate knowledge of two- and three-dimensional profiles are required in order to predict device performance and reliability. Corroboration of process simulator predictions of heterostructure and dopant profiles, with the actual profiles themselves, therefore becomes increasingly important as sub-micrometer dimensions are achieved in manufacturing practice. Failure analysis has heretofore been the object of relatively few scanned probe microscope (SPM) studies. Our application of SPM to failure analysis is a natural extension of the metrological applications of AFM which have been made during the past several years. For both dopant profiling and failure analysis, we have sought to develop a technique which, as much as possible is relatively fast, requires minimum sample preparation, is non-destructive, sensitive, accurate, and reproducible.

Reviews of dopant profiling techniques have been presented [1,2] elsewhere. Techniques specific to 2D dopant profiling are important in comparison with our work. Secondary-ion mass spectrometry (SIMS) is used in conjunction with samples beveled on multiple angles [3], or etched in vertical relief at an angle to an implanted edge [4], in order to obtain 2D information. SIMS techniques require multiple samples for each dopant profile. Optical techniques, combined with sample etching and beveling, detail profiles in the 10^{14}–10^{19} cm^{-3} range, with lateral resolution of 40 nm [5]. Scanning capacitance microscopy (SCM) [6–9] requires little sample preparation. Depletion regions limit lateral resolution to roughly 50 nm, though contrast on the scale of 10 nm can be observed. Computer data deconvolution has been used. Best results require a fit of data to

* Corresponding author. Redwood Microsystems, Inc., 1020 Hamilton Avenue, Menlo Park, CA 94025 USA. Tel.: +1 415 6170854; fax: +1 415 3269217; e-mail: henning@redwoodmicro.com

Published by Elsevier Science S.A.
PII S0921-5107(96)01688-1

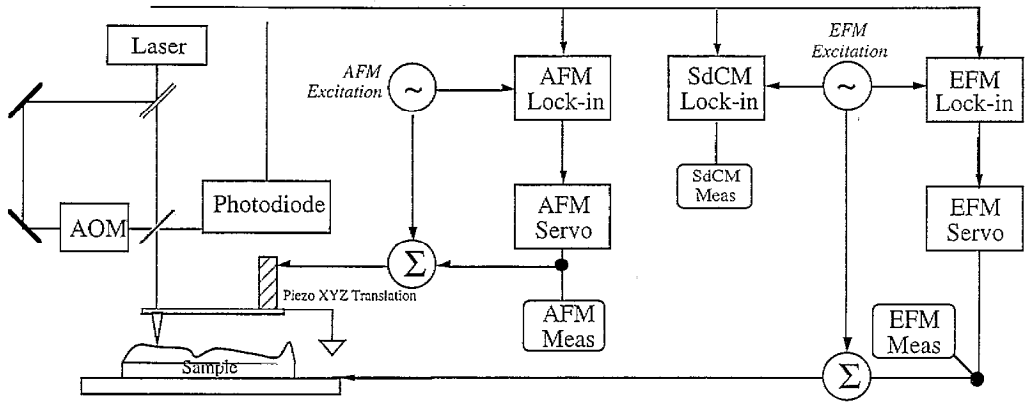

Fig. 1. Schematic of the SPM system described in this work. There are three measurement modes: atomic force (AFM); electrostatic force (EFM); and differential capacitance (SdCM). The AFM and EFM modes incorporate closed-loop feedback. Measurements are derived from monitoring the magnitude (peak-to-peak) of the mechanical oscillation of the cantilever probe in response to mechanical and electrical excitations. The monitoring scheme is based on heterodyne techniques [32], where an acousto-optical modulator (AOM) imposes an acoustic frequency atop a laser carrier frequency of 633 nm wavelength.

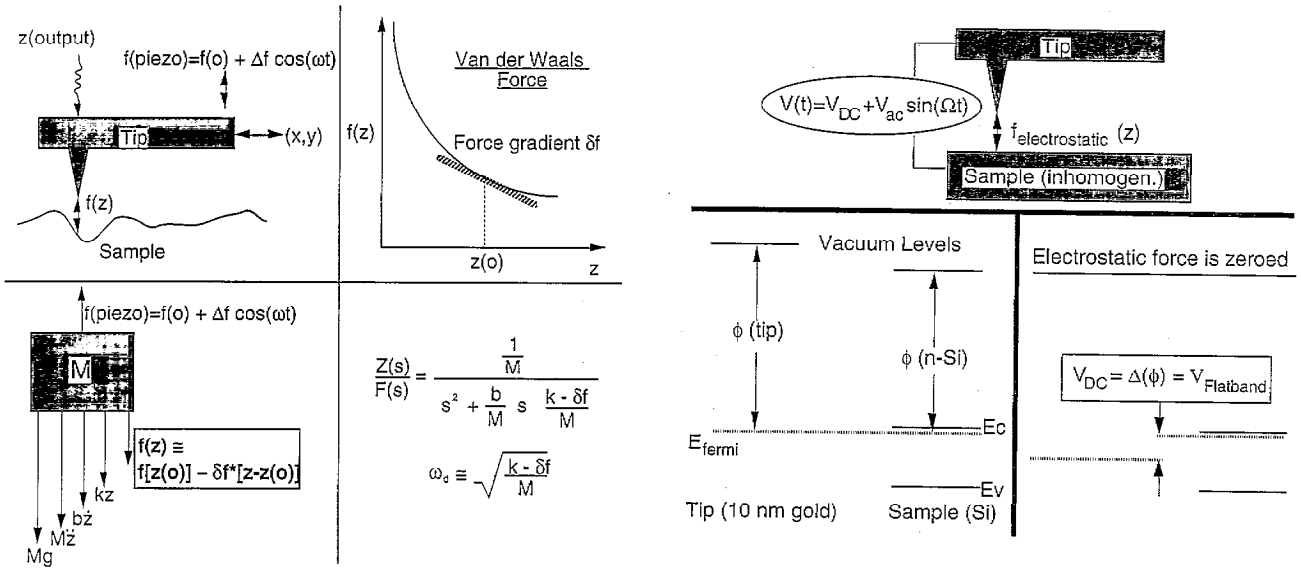

Fig. 2. (a) Upper left: schematic of the AFM mode of cantilever probe behavior. Upper right: schematic of the attractive atomic force, including the operating point $z(0)$ of the system. Lower left: one-dimensional free-body diagram of the cantilever response, showing linearized atomic force. Lower right: linearized system model equation. The effect of the Van der Waals force gradient is to reduce the apparent, damped resonance frequency. (b) Upper: schematic of the EFM mode of cantilever probe behavior. Lower left: one-dimensional band diagram of the electrostatic system, for $V(\mathrm{DC}) = 0$. Lower right: one-dimensional band diagram of the electrostatic system, for $V(\mathrm{DC})$ equal to the flatband voltage, yielding zero electrostatic force loading on the cantilever.

a parameter related to the dielectric constant of water. Imaging of dopant profiles for semiconductor surfaces lying beneath significant thicknesses of insulator is difficult. Inference techniques for obtaining 2D profiles couple process simulation, and measurement of source-drain overlap capacitance [10]. Extraction of dopant profiles is subject to the specifics of the simulation transport and capacitance models. Spreading resistance combined with mechanical magnification using angled and beveled etching has recently achieved 10^{12} cm^{-3} sensitivity with 25–50 nm lateral spatial resolution [11]. Computer deconvolution of the data is required. AFM measurements of cross-sectioned junctions decorated with a dopant concentration-sensitive etch [12,13] provide well-resolved images of simple MOSFET dopant profiles. The etch process is destructive, and best suited to cross-sectioned samples. Scanning resistive microscopy [14] has been applied recently to the profiling of dopants in thin, uniformly doped, conductive layers. Spatial resolution presently is greater than 100 nm.

The use of SPM for failure analysis derives from the use of AFM and scanning tunneling microscopy (STM) in metrological studies of microelectronic materials and

structures. Structures imaged include, but are not limited to, photoresist topography, and silicon dioxide surface roughness [15–17]. SPM techniques have also been used to image electronic signals in active microelectronic circuits [18–20].

The remainder of this paper will focus on three areas. Measurement techniques are first described briefly. Principal results of our investigations are presented next. Finally, some limitations of the SPM techniques in extracting quantitative information are detailed, along with suggestions for means to improve upon them.

2. Description of measurement techniques

Full details of our techniques can be found elsewhere [21,22]. Here, we will highlight the most important aspects of our measurement system.

Simply put, a micro-machined cantilever is rastered across the sample surface. Mechanical and electrical excitations are applied to the cantilever, at different frequencies. The amplitude of the cantilever oscillation responding to the excitations at each of these frequencies is measured. This amplitude is related to the specific forces of interaction between the cantilever tip and the sample surface.

Fig. 1 shows a schematic of our SPM system. Three modes are measured simultaneously. Separate lock-in feedback loops enable measurement of surface topography (AFM) and surface work function (EFM). An open-loop measurement allows detection of sub-surface charge (SdCM). A laser heterodyne interferometer is used to monitor the relative position of the microscope tip above the sample surface.

For the AFM measurement (see Fig. 2(a)), the mean DC position of the cantilever tip above the surface is kept constant as the tip is rastered. The cantilever is excited mechanically at a frequency ω slightly above its fundamental resonance frequency (see Fig. 3). As the lateral position changes, the distance between tip and surface first changes. This change alters the van der Waals force, which increases or decreases the oscillation amplitude at the mechanical excitation frequency. The mean DC position is increased or decreased until the original oscillation amplitude is recovered. The DC cantilever position is then recorded, and the cantilever tip moves to the next raster position, until the full image of topography is extracted.

For the EFM measurement (see Fig. 2(b)), the force-based Kelvin method is employed [23]. The electrical force excitation frequency Ω is chosen to correspond to a different normal mode of mechanical oscillation than that used for the AFM measurement (see Fig. 3). In the absence of any DC voltage between the cantilever tip and the sample surface, the work function difference between the materials comprising the tip-surface system yields an electrostatic force. The work function difference is dependent upon doping if one of the materials is a semiconductor [24]. If a DC flatband voltage is applied, the electrostatic force will be nulled and the ac oscillation amplitude will be minimized. At each lateral position, the value of this voltage which minimizes or nulls the mechanical oscillation amplitude is recorded.

The SdCM mode occurs as a consequence of the EFM mode. The electrostatic force is related to the derivative of the electrostatic energy with respect to the relative position of the tip above the surface, $F \sim dE/dz$. But the electrostatic energy is proportional to the square of the applied voltage, $E \sim CV^2$. Since $V(t) = V_{DC} + V_{ac}\sin(\Omega t)$, there is a detectable signal, a mechanical excitation, proportional to the derivative of the total series capacitance C with respect to distance, which occurs at a frequency twice that of the ac component of the applied voltage.

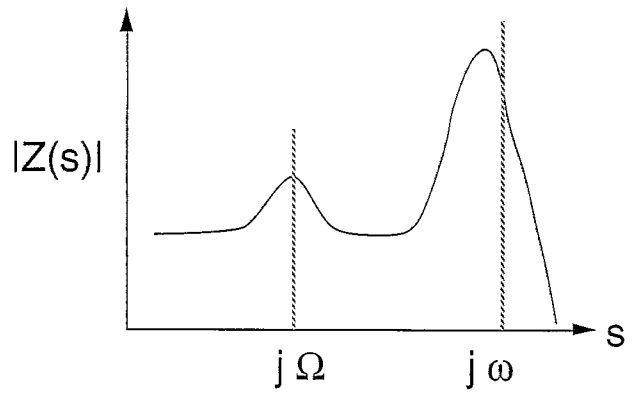

Fig. 3. Schematic representation of the mechanical transfer function of the cantilever probe. Two peaks are used for the detection of cantilever oscillation. The frequency ω corresponds to the AFM mechanical excitation, while the frequency Ω corresponds to the EFM electrical excitation.

3. Results and discussion

Our application of this three-mode measurement system has been documented elsewhere [21,22,25–27]. We review the principal results in this section.

In the area of dopant profiling, we first measured simple dopant structures [21]. To perform these measurements, n-type (phosphorus) substrates were first oxidized in dry O_2. Then, 2.5×2.5 μm contact holes and stripes were fabricated into a photoresist layer. A blanket Boron implant followed next. The samples were dipped in dilute HF, and the photoresist was stripped. They were then oxidized at 900°C for 20 min in dry O_2. They received little preparation for measurement. Some were simply cleaned in deionized water. The samples shown here received a 2 min dip in 100:1 dilute HF.

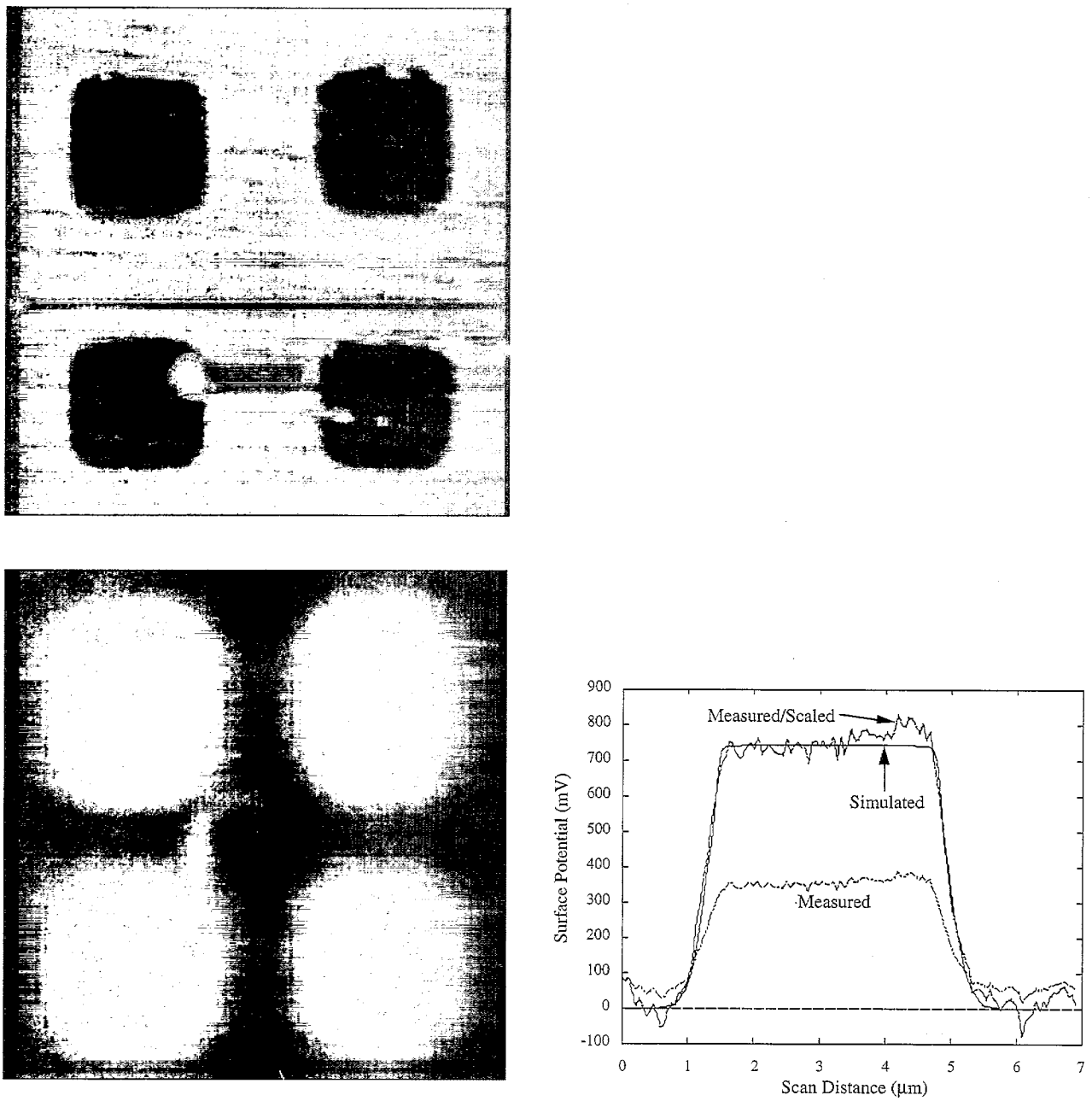

Fig. 4. (a) Greyscale images of doped silicon experiment. Left: AFM (topographic) image. Right: EFM image, showing dispersion of the boron dopant relative to the implant edge. (b) Comparison of measured surface potential, and 3D simulation of the surface potential based on simulated dopant diffusion.

Fig. 4(a) shows greyscale images of some of the results. The AFM images show the relatively sharp edges which correspond to an 8–11 nm step in the silicon substrate, which occurred due to the oxidation differences between the lightly-doped n-type substrate, and the heavily-doped implanted regions. The EFM images show qualitatively how the dopant has diffused outward from these implantation edges.

A line scan through the center of one of the contact structures is shown in Fig. 4(b), along with a simulated scan (derived from a solution to Poisson's equation using the finite element simulator FIELDAY [28]), and a scaled replica of the measured scan. The measurement and simulation have the same linewidth, corresponding to the change in dopant type from n to p, and the change in dopant magnitude. However, the measurement falls below the simulation. Scaling the measurement shows good quantitative agreement between measurement and simulation. The source of the scaling factor (the source of the reduced measurement signal

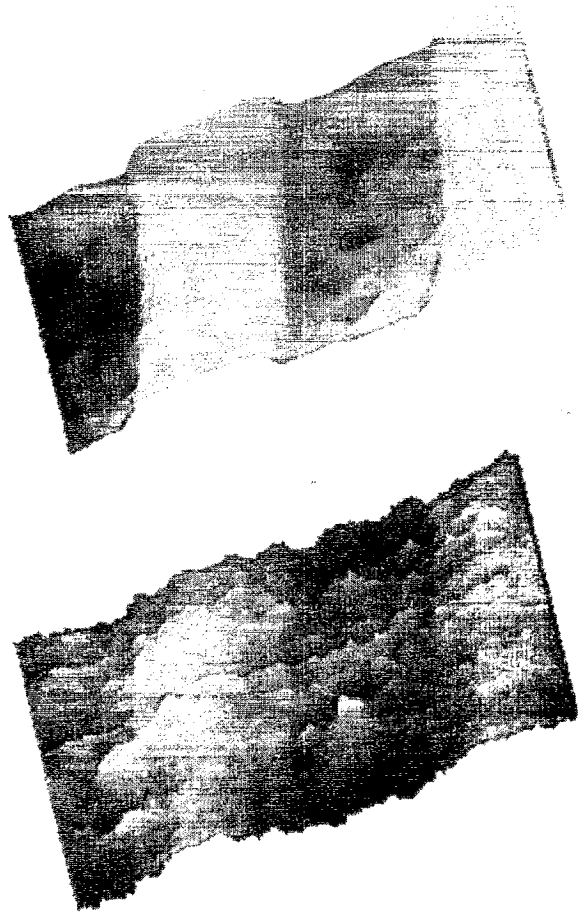

Fig. 5. Greyscale images of the lightly-doped drain MOSFET structure. Top: AFM image of n-MOSFET channel, including tungsten source-drain contact plug residue. Bottom: EFM image of the surface potential related to dopant profiles. Note the clear shelf between the channel doping, and the heaviest source-drain doping, corresponding to the LDD region.

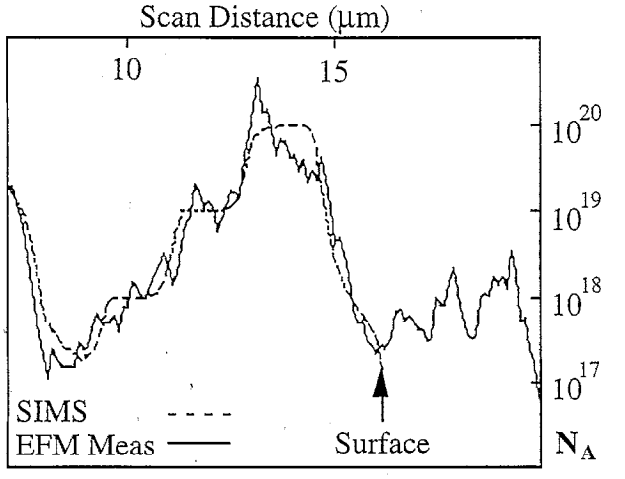

Fig. 6. Doping profiles for SEMATECH round-robin sample, measured using SIMS, and the force-based Kelvin method (EFM). The sample was beveled prior to EFM measurement, to obtain mechanical magnification. The bevel angle is 2°.

versus simulated profile) will be discussed in the next section.

One of the key dopant structures in microelectronic devices is the lightly-doped drain (LDD) structure, which reduces peak electric fields in MOSFETs, and so improves reliability by reducing device degradation via hot electron or hole injection. Prior to our work, the LDD structure had not been imaged via direct means, making design and realization of LDD structures matters of speculation and inference, from simulation and electrical parametric data. We have been able to measure LDD structures, in n- and p-channel MOSFETs, along device surfaces as well as in cross-section. Fig. 5 shows AFM and EFM images of one such n-channel MOSFET device. The samples were prepared by fabricating complete MOSFET devices, then stripping the surface layers down to the bare silicon via a series of etching steps. The AFM image shows the smooth surface associated with the gate oxide (channel) layer. Rougher surfaces to either side lie above the heavily doped source-drain regions, due either to the higher oxidation rate for heavily doped silicon (versus the more lightly doped channel), or the use of a silicide in the source-drain region. Dark circles in the source-drain regions correspond to tungsten contact plugs. The EFM image shows the channel, LDD, and heavily-doped source-drain regions. Vertical position (contrast intensity) corresponds to dopant type and magnitude. The LDD region is the 'shelf' which parallels the channel region. Note the asperities in dopant in the channel region. These may be due to dopant density anomalies in Boron-doped channel.

The driving force of miniaturization will reduce microelectronic device minimum features to 0.1 μm by the year 2004 [29]. As a result, the U.S. semiconductor consortium SEMATECH has issued a set of Grand Challenges which must be met in order to achieve this goal. Metrology, and the need to measure dopant profiles in 2D and 3D, are high on the list of these challenges. Consequently, we participated in a 'round-robin' set of experiments, in order to assess tools to measure dopant profiles with the spatial resolution, and accuracy in dopant concentration, necessary to meet industry's needs. One of the test structures consisted of a series of epitaxial layers of doped silicon, grown on a silicon substrate. Each layer had a different designed dopant concentration. Along with researchers of other dopant profiling techniques, we were asked to use our methods to determine the dopant profiles, and compare our results with simulation and SIMS measurements. We beveled the sample in order to achieve mechanical magnification of the profile, and polished it according to proven techniques [30]. Some of our results are shown in Fig. 6. They indicate some success using our methods. In particular, we obtain good qualitative results. However, in the absence of data decon-

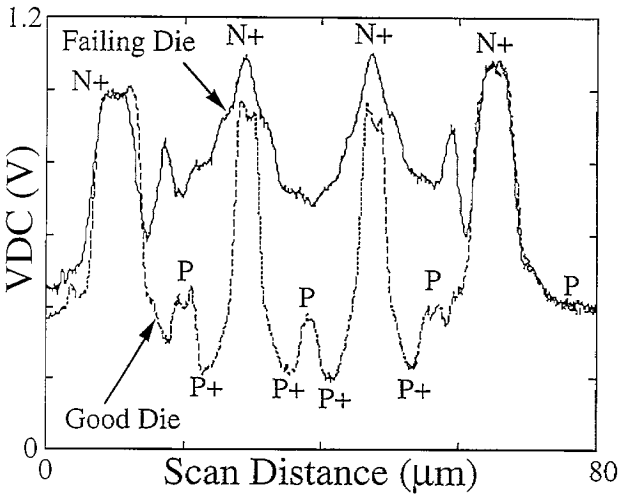

Fig. 7. Measurements of doping profiles in BiCMOS devices. The ability to measure dopant is here used to identify physical device failure mechanisms. Here, the absence of a p-type well implant was observed in failing die.

volution, true small-signal measurement, and parasitic capacitances, extraction of full, quantitative dopant profiles is not possible as yet using our method.

Our methods have found perhaps their greatest success in the arena of failure analysis. The ability to measure dopant profiles can also be used to extract information about device and material failure. Fig. 7 shows a first example. Our IBM colleagues monitored a certain BiCMOS process using current vs. voltage measurements, and discovered anomalies which suggested a missing well implant. We used our imaging methods to compare good devices (lower curve) against failing devices (upper curve), and were able to demonstrate unequivocally the absence of the well implant, confirming physically the speculations from parametric tests.

As transistor densities increase, circuit designers seek increasingly to pack more transistors into shrinking space. As a result, transistors are not laid out along the principal [100] crystal axes, but frequently are laid out along [110] axes. In order to control design performance, designers must have knowledge of how the channel length (determined by diffusion coefficient) varies as a function of crystal orientation. For larger scale devices, the theoretical, isotropic nature of dopant diffusion in the face-centered cubic silicon crystal has held true. However, as minimum feature sizes shrink, we have shown that MOSFET channel lengths, determined by dopant diffusion, are not independent of crystal orientation. Fig. 8 shows AFM and EFM comparisons of [100] and [110] oriented MOSFETs. The AFM image confirms that the physical positions of the channels, as determined by the change in surface topography, are the same. The EFM image, however, shows that the [100] channel lengths are shorter than the [110] channels. This difference suggests that some point defect mechanism of dopant diffusion is orientation dependent. We believe this difference is due to the dependence of oxidation rate on crystal orientation, with its commensurate difference in point defect injection at the edge of the MOSFET. Our measurements were performed on a large number of samples, with a variety of channel lengths. The results were consistent, and statistically significant.

Again in conjunction with IBM, we demonstrated the ability of our methods to determine dynamic random access memory (DRAM) failures due to ionic contamination. Fig. 9 shows the images obtained via our experimental process. Two sets of DRAM cells were identified, one demonstrating the cell failure at electrical test, one not. AFM images for both samples were identical showing the defect was not topographic in nature. EFM images were also inconclusive. However, the SdCM images, being sensitive to changes in capaci-

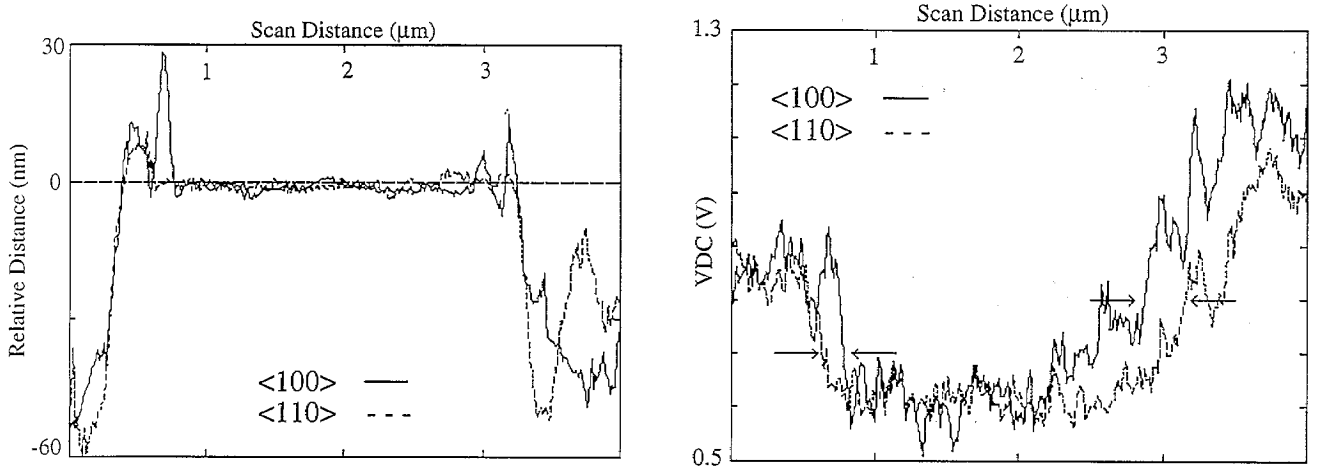

Fig. 8. Line scans of ⟨100⟩ and ⟨110⟩ MOSFET channels. Upper: AFM scan, showing no crystal orientation difference of the physical channel length. Lower: EFM scan, showing clear channel shortening for the ⟨100⟩ device, as defined by the edge of the dopant profile controlling the device electrical behavior (arrows).

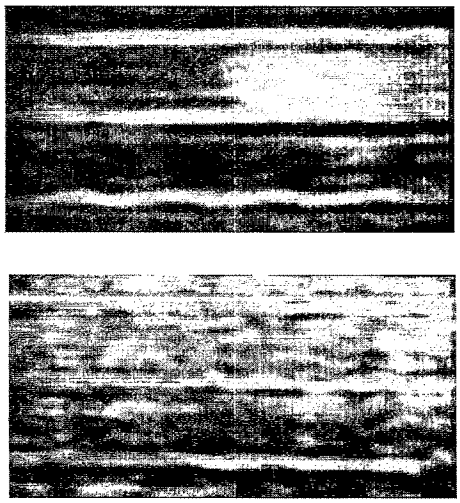

Fig. 9. Greyscale images of ionic defect in DRAM memory cell. Upper: SdCM image prior to bake. The bright spot corresponds to a sub-surface charged ion defect. The size of the spot varied as a function of ac bias V(ac). Lower: SdCM post-bake. After an elevated-temperature bake cycle, the ionic defect was no longer perceptible using SdCM.

tance due to sub-surface charge, showed a feature in the failing cells not noted in the passing cells. The image of this feature increased or decreased as a function of the magnitude of V_{ac}. Attributing the feature to a mobile ionic charge, we baked both samples, and repeated the measurement. If ionic in nature, we reasoned the defects would disappear, as they dispersed during the baking process. As shown, the defect did disappear upon subsequent measurement. Our discovery led to process changes which eliminated this DRAM failure mode.

Random access memories (RAMs) experience dopant-related defects which lead to device failure. As gate oxide thicknesses decrease, commensurate with smaller feature sizes, dopants from the polysilicon gate can diffuse through the gate oxide and compensate the channel dopant, reducing threshold voltages and increasing currents in an unwanted manner. Fig. 10 shows our use of SdCM to determine this failure mode. Passing and failing samples, determined from electrical parametric test once more, was stripped back to their polysilicon gate layers, and then measured in our system. Failing gates showed a marked change in contrast (lower gate in the SdCM scan), compared with unfailing gates (upper gate in the SdCM scan), consistent with the diffusion of (in this case) Boron from the polysilicon, into the n-typed doped MOSFET channel. Note that both gates, in both AFM and EFM scans, are virtually identical. The ability to detect such defects beneath significant overlayer thicknesses is nearly unique to our method.

Our EFM technique relies on the force-based Kelvin method. As such, the physical property measured is, strictly speaking, the surface work function, and not the dopant density. This feature, however, can be used to measure semiconductors under stress. Stress, either compressional or tensile, will alter the band gap, which in turn will alter the work function. Fig. 11 shows an example of this type of measurement. Polysilicon gates in MOSFETs typically continue past the channel, and up onto the surrounding field oxide, in order to defeat electrical leakage around the side of the channel regions. The process of creating this structure involves growing the thick field oxide underneath the end of the polysilicon gate. As this growth proceeds, the polysilicon line is bent upward, creating compressional stress in the surface, and tensile stress beneath. The stress appears as a constant change (bright spot on the left, at the edge of the LOCOS field isolation oxide) in our EFM images, which does not appear in either the AFM or SdCM images.

Our system can also image crystal defects. Fig. 12 shows one set of defect measurements. The defects bridge across active transistor layers (surface layers have been removed prior to our measurement). While somewhat apparent in the EFM mode, these crystal defects were more apparent using AFM, and most apparent in the SdCM mode. The presence of these crystal defects was confirmed using more conventional TEM techniques. Note here, too, the loop dislocation seen in Fig. 4(a). It is not certain whether the imaging

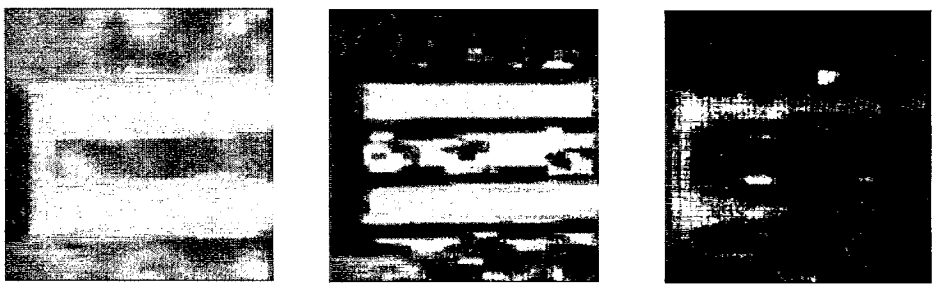

Fig. 10. Greyscale images of random access memory cells, showing ability of the SdCM mode to image dopant defects beneath a stack of insulators and conductors. Left: AFM image showing no discernible topographic difference between the good (upper) gate, and the failing gate (lower). Middle: SdCM image showing lower gate has experienced boron encroachment from the polysilicon gate, into the device channel (brighter contrast). Right: EFM image, as with AFM showing no discernible difference attributable to surface potential.

force related to the loop is due to stress-related work function differences; or, to Boron atoms which have decorated the loop via preferential diffusion, leading again to detectable work function differences.

4. Obstacles to quantitative measurement

The combination of AFM, EFM, and SdCM has the clear ability to measure dopant profiles, and to image and identify microstructure failure mechanisms. However, as we have noted already, our microcantilever detector has certain aspects which require improvement, in order that fully quantitative measurement of dopant profiles can be achieved. We have detailed only some of these aspects elsewhere [22,26,31], leaving much of the information in this section as new information. This section focuses on three of the main barriers: parasitic capacitance; deconvolution; and large-signal effects of V_{ac}.

The effect of parasitic capacitance between the cantilever and the substrate upon the measurements can be quite dramatic. Fig. 13 shows one part of this effect. Our force-detection methodology presumes the only important force coupling between the cantilever and the substrate is through the cantilever tip. The assumption is that, while the tip area of interaction is small, its separation from the surface is so small that the force coupling here will overwhelm any parasitics. We have demonstrated this may not be the case, especially for the relatively long-ranged electrostatic force coupling. In obtaining EFM images of arrays of doped contact holes, we noted an abnormal rise in signal near hole edges. We then performed simulations in order to determine if parasitic force coupling could explain the phenomenon. In fact, we were able to reproduce qualitatively the same type of edge-related signal increases, which are also shown in Fig. 13.

Convolution is an inherent part of our measurement. Atomic and electrostatic forces couple the cantilever tip to surface 'pixels'. Pixels directly beneath the tip, and those in the vicinity of the tip, all provide force contributions to the detector. Our dopant profile extraction method assumes that all force coupling is between the tip and the pixel directly beneath the tip. This assumption places constraints on the ability to extract quantitative, 2D information of dopant concentration. Fig. 14 shows the extent of the problem. Based on the SEMATECH sample of Fig. 7, we compare a simulation of a dopant profile with the SIMS profile of the sample. The simulation in this case assumes that multiple pixels in the vicinity of the measurement position (x, y) contribute to the measured signal. The dopant concentration (and electrostatic force coupling) is not assumed to be constant for each pixel. As a result, there is a smearing of the dopant profile, extracted using our one-pixel assumption, when compared with the actual profile. We observe such smearing in Fig. 6, demonstrating the need to incorporate deconvolution in order to sharpen the actual doping profile from the measured signals.

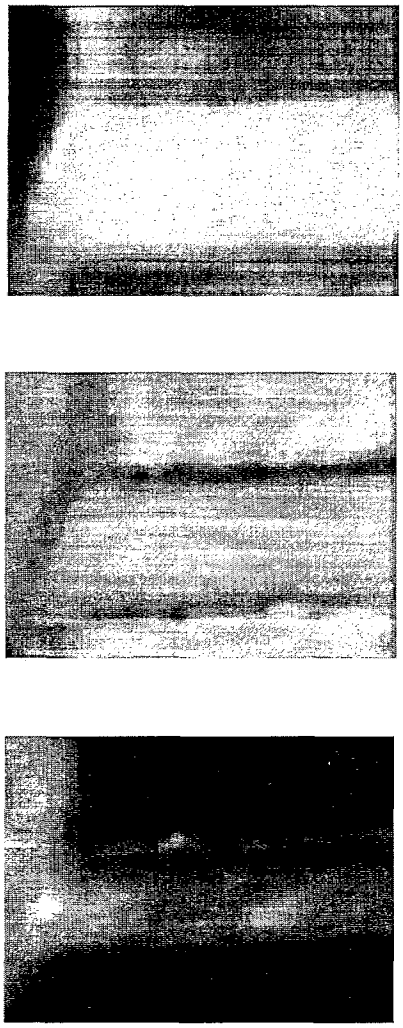

Fig. 11. Greyscale images of random access memory cells, showing ability of the EFM mode to image stress-related changes in polysilicon work function due to field oxide growth. Top: AFM image showing no discernible topographic variations across the length of the gate. Middle: SdCM image showing, similarly, no variations. Bottom: EFM image, showing contrast change at the field oxide/channel boundary. This change occurs due to stress concentration at this boundary: as the polysilicon is bent upward, the band gap in this region decreases, causing observable changes in the work function at this point.

In extracting information from our EFM and SdCM techniques, we presume the applied voltage V_{ac} is small-signal in nature, leading to a linear analysis. In practice, this presumption is not true. V_{ac} can be large, on the order of volts. The need for large V_{ac} depends upon the strength of the EFM and SdCM signals obtained for a particular sample. Fig. 15(a) shows how increases in V_{ac}

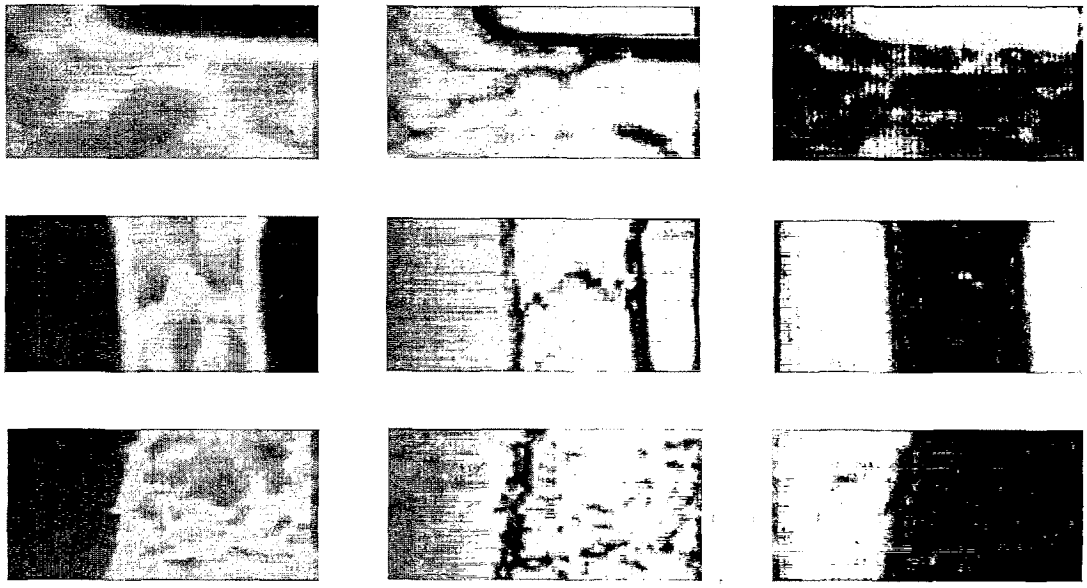

Fig. 12. Greyscale images of dislocation defects in random access memory cells. Boundaries are between active areas and thick-oxide isolation areas. The defects occur in the active regions. Left column: AFM images showing some evidence of defects. Center column SdCM images, showing greatest contrast imaging of the defects. Right column: EFM images, showing limited evidence of the defects.

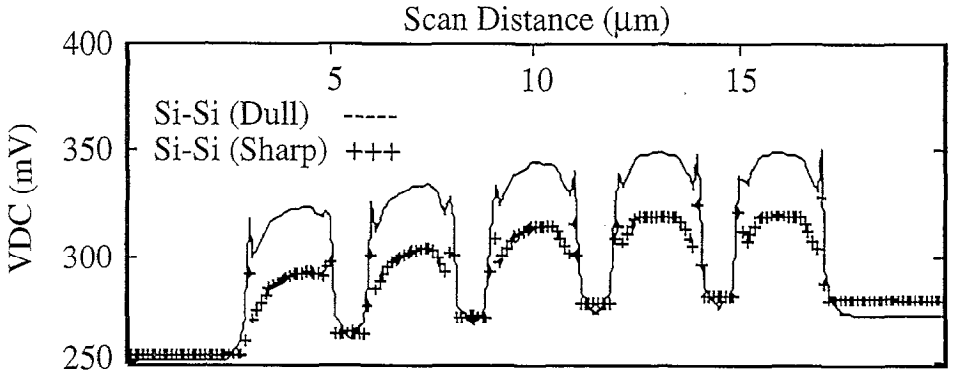

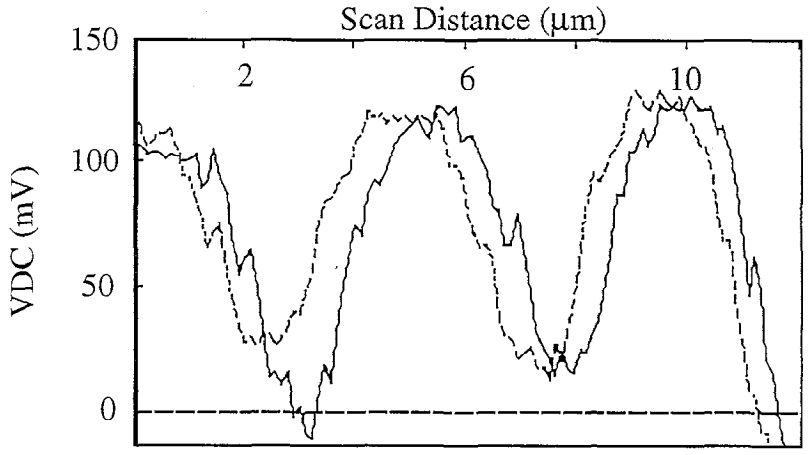

Fig. 13. Simulation and measurement of the effect of parasitic capacitive coupling between the cantilever and the surface. Upper: simulation showing the 'bat ears' signature of parasitic coupling. The probe tip is assumed to be silicon, as is the substrate. Sharper tips cause greater contrast in measured work function difference between regions of different dopant type. The rise in the baseline of the signal is due to the increased electrostatic coupling between the substrate and the cantilever, as more dopant stripes lie beneath the cantilever. Lower: measurement of a cantilever passing over alternative lines of doped silicon. Note the signatures of parasitic coupling at the line edges. Note also the rise in the signal

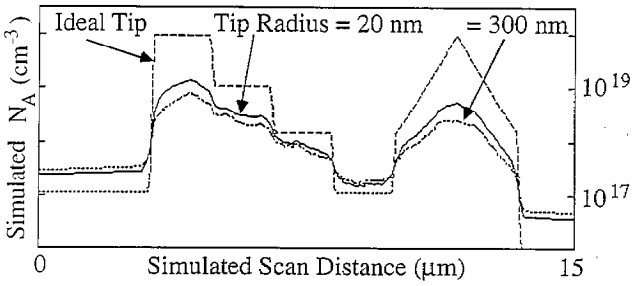

Fig. 14. Simulation of the effect of probe radius on the ability to resolve fully, large changes in doping over small distances. (Compare with Fig. 6, where this effect is observed experimentally.)

can obscure the nature of the work function difference between the sample surface and the cantilever tip. We measured a surface with uniform material composition, using tips with differing compositions, as a function of V_{ac}. We observed the signal differences to be greatest, as expected, for smallest V_{ac}. These differences disappeared as V_{ac} increased.

With respect to dopant profiling, this effect can be seen in Fig. 4(b), where V_{ac} was relatively large, and decreases the apparent dopant concentration extracted from the EFM signal. This effect is explained in Fig. 15(b). The application of V_{ac} to the cantilever tip causes the potential of a semiconductor surface to vary as a function of time. Consider two such surfaces, with different dopant concentrations, and so different surface work functions and different flatband voltages. For V_{ac} small compared with the semiconductor band gap, the surface potentials oscillate as a function of time, but are still separated in electrostatic energy. This energy difference will be in direct relation to the dopant concentration difference, and no loss of signal will result. However, if V_{ac} becomes large, the surface potential will not follow the full excursion imposed by V_{ac}, due to the pinning of the conduction and valence bands at the Fermi level during each oscillation. As a consequence, signals from the two samples become indistinguishable, even though they have different dopant concentrations. The ability of a semiconductor surface

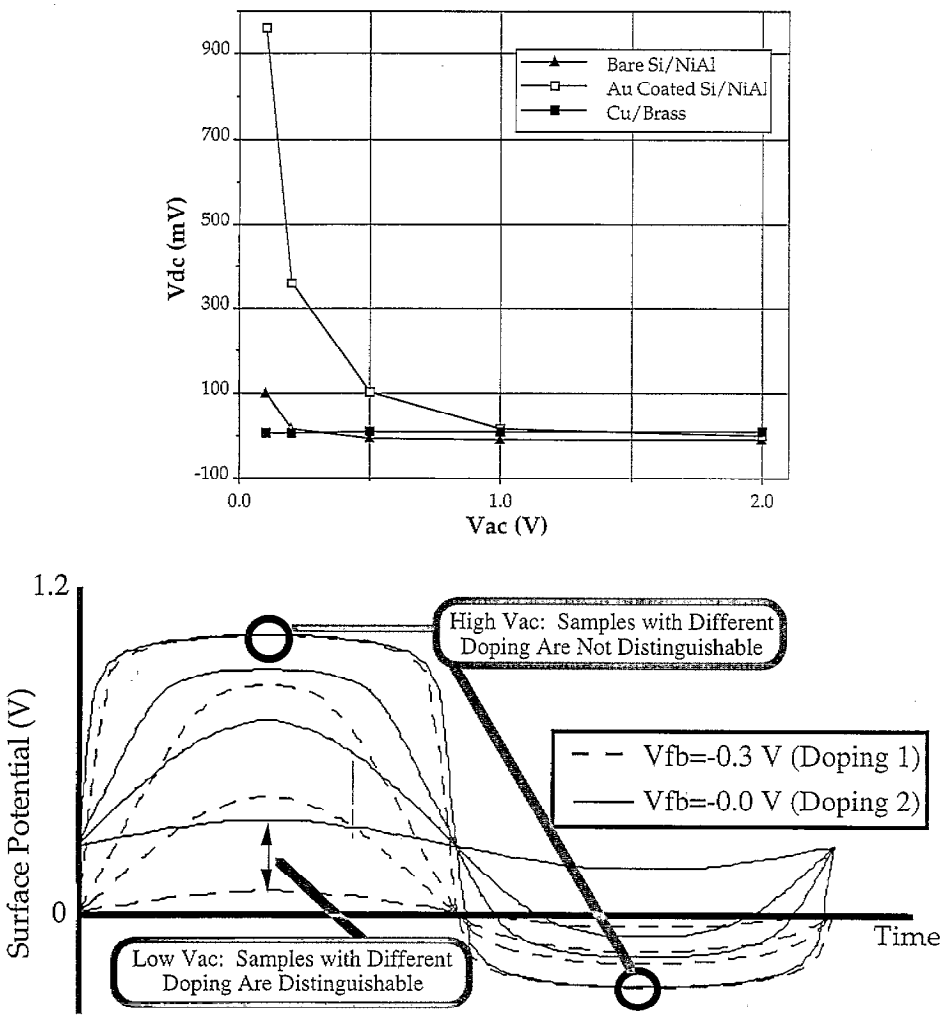

Fig. 15. Upper: measured dependence of V(DC) on the magnitude of V(ac). Lower: simulation of time dependence of semiconductor surface bands, as a function of doping and V(ac).

to respond fully to V_{ac}, therefore, depends strongly on the magnitude of V_{ac} compared with the band gap. From a system perspective, increasing detector sensitivity in order to allow smaller V_{ac} becomes an important goal.

5. Conclusions

Our work has broken new ground in the use of SPM techniques in both dopant profiling, and in microfabricated device and materials failure analysis. We have advanced the state of the art of the force-based Kelvin method, in extracting dopant profiles from semiconductor materials in structures of high technological interest. As a result, this method is a leading candidate (along with SCM) to measure dopant profiles with the spatial resolution and accuracy required by the semiconductor industry. Our use of AFM, EFM, and SdCM has also shown great promise in the area of failure analysis. This combination of techniques allows simultaneous detection of inhomogeneities in surface topography, surface work function, and sub-surface charge. As a result, samples with minimum surface preparation can be measured quickly. Information concerning roughness, stress- or dopant- or material-related work function, and charge can be extracted in short order. Rapid failure assessment, compared with conventional techniques, thus becomes possible and practical. And, structures otherwise impossible to assess for failure can be imaged for the first time.

Our work has also demonstrated quantitatively the scientific limitations of SPM techniques for dopant profiling and failure analysis applications. Parasitic capacitance, data convolution and large-signal effects must be reduced or eliminated, in order for these techniques to reach their maximum potential benefit.

Acknowledgements

The authors acknowledge with gratitude and deep respect, the collaboration and support of research colleagues in this work over the past four years: at Dartmouth, Charles Daghlian and Christopher G. Levey; at IBM in Essez Junction, VT, Jim Slinkman, Steve Hoffman, Jim Never, Phil Kaszuba, and Pepi Cadrecha. Research support through an IBM Shared University Research Grant, an Analog Devices (Inc.) Career Development Professorship, and a Thayer School graduate fellowship, are also acknowledged with gratitude.

References

[1] C. Hill, *Proc. Euro. Solid State Device Research Conference*, Adam Hilger, Bristol, UK, 1990, p. 53.
[2] R. Subrahmanyan, *J. Vac. Sci. Technol. B, 10* (1992) 358.
[3] S.H. Goodwin-Johansson et al., *J. Vac. Sci. Technol. B, 10* (1992) 369.
[4] M.G. Dowsett and G.A. Cooke, *J. Vac. Sci. Technol. B, 10* (1992) 353.
[5] R. Subrahmanyan, H.Z. Massoud and R.B. Fair, *J. Electrochem. Soc., 137* (1990) 1573.
[6] C.C. Williams et al., *Appl. Phys. Lett., 55* (1989) 1662.
[7] J. Slinkman et al., *International Electron Devices Meeting, Dig. Tech. Pup.*, IEEE, Piscataway, NJ, 1990, p. 73.
[8] G. Neubauer et al., *J. Vac. Sci. Technol. B, 14* (1996) 426.
[9] J.J. Kopanski, J.F. Marchiando and J.R. Lowney, *J. Vac. Sci. Technol. B, 14* (1996) 242.
[10] N. Khalil et al., *IEEE Elec. Dev. Lett., 16* (1995) 17.
[11] T. Takigami and M. Tanimoto, *App. Phys. Lett., 58* (1991) 2288.
[12] R. Avis et al., *J. Vac. Sci. Technol. B, 14* (1996) 231.
[13] M. Barrett et al., *IEEE Elec. Dev. Lett., 16* (1995) 118.
[14] C. Shafai et al., *Appl. Phys. Lett., 64* (1994) 342.
[15] C.B. Prater et al., *J. Vac. Sci. Technol. B, 10* (1992) 1211.
[16] T. Ohmi et al., *IEEE Trans. Elec. Dev., 39* (1992) 537.
[17] S. Gwo et al., *Appl. Phys. Lett., 61* (1992) 1104.
[18] G.E. Bridges, T.S. Forzley and D.J. Thomson, *Microelectron. J., 23* (1992) 363.
[19] C. Böhm et al., *J. Phys. D, 26* (1993) 1801.
[20] B.A. Nechay et al., *J. Vac. Sci. Technol. B, 13* (1995) 1369.
[21] A.K. Henning et al., *J. Appl. Phys., 77* (1995) 1888.
[22] T. Hochwitz, Implementation, Characterization, and Applications of a Scanning Kelvin Probe Force Microscope. *PhD Dissertation*, Dartmouth College, Hanover, NH, 1996.
[23] M. Nonnenmacher, M.P. O'Boyle and H.K. Wickramasinghe, *Appl. Phys. Lett., 58* (1991) 2921.
[24] S. Sze, *The Physics of Semiconductor Devices*, Wiley, New York, 1981.
[25] T. Hochwitz et al., *J. Vac. Sci. Technol. B, 14* (1996) 440.
[26] T. Hochwitz et al., *J. Vac Sci. Technol. B, 14* (1996) 457.
[27] T. Hochwitz et al., *Proc. Int. Reliability Physics Symposium*, IEEE, Piscataway, NJ, 1995, p. 217.
[28] K.A. Salsburg, P.E. Cottrell and E.M. Buturla, *Proc. NATO Adv. Study Inst. on Process and Device Simulation of MOS-VLSI Circuits*, Martinus Nijhoff, The Hague, 1983, p. 582.
[29] *National technology roadmap for semiconductors*, Semiconductor Industry Association, San Jose, CA, 1994.
[30] J. Never, IBM Corporation, Essex Junction, VT. Private communication; P. Kaszuba *ISTFA '95: Proc. 21st Int. Symp. Testing and Failure Analysis*, ASM International, Materials Park, OH, 1995.
[31] A.K. Henning, *Proc. Microlithography and Metrology in Micromachining*, Vol. 2640, SPIE, Bellingham, WA, 1995, pp. 236–245.
[32] H.K. Wickramasinghe et al., *J. Phys. Coll., 44* (C-6) (1983) 191.